Emergent tricriticality in magnetic metamaterials

Björn Erik Skovdal [○],[1] Gunnar K. Pálsson [○],[1] P. C. W. Holdsworth,[2] and Björgvin Hjörvarsson [○][1,*]

[1]*Department of Physics and Astronomy, Uppsala University, Box 516, 751 20 Uppsala, Sweden*
[2]*Université de Lyon, ENS de Lyon, CNRS, Laboratoire de Physique, 69342 Lyon, France*

Metallic disks engineered on the 100 nm scale have an internal magnetic texture which varies from a fully magnetized state to a vortex state with zero moment. The interplay between this internal structure and the interdisk interactions is studied in magnetic metamaterials made of square arrays of the magnetic disks. The texture is modeled by a mesospin of varying length with $O(2)$ symmetry and the interdisk interaction by a nearest-neighbor coupling between mesospins. The thermodynamic properties of the model are studied numerically and an ordering transition is found which varies from Kosterlitz-Thouless to first order via an apparent tricritical point. The effective critical exponent characterizing the finite-size magnetization evolves from the value for the 2D XY model to less than half this value at the tricritical point. The consequences for future experiments both in and out of equilibrium are discussed.

I. INTRODUCTION

Universality, phase transitions, and emergent magnetic properties are examples of phenomena that have recently been explored in metamaterials [1–10]. The ability to choose and investigate the effect of a single parameter, such as spin or spatial dimensionality [2–4,9], as well as the possibility to directly observe individual magnetic elements, has been a major impetus in this context [11–18]. These are indicators that nanoengineered materials can, in analogy with cold atom systems, become simulators of model many-body problems, offering clear advantages over traditional condensed matter systems operating on the atomic scale. In this regard, metamaterials made up of magnetostatically interacting mesoscale islands, or *mesospins*, are highly attractive. The multiscale nature of the experimental setup allows for the emergence of new degrees of freedom from the internal spin textures, giving rise to rich behavior beyond that of standard magnetic models [19–25]. Mesoscopic arrays of circular magnetic islands show a vast ensemble of internal magnetic textures, which vary strongly with the local environment. One of the most characteristic textures is a vortex which can progressively unwind from a state with zero magnetic moment into a collinear state with maximal moment [26].

The change from vortex to collinear states was shown to be driven by a competition between inter- and intraisland interactions so that in an emergent description the interactions between mesospins are self-consistently modified by the collective environment [26]. As a consequence, mesospin ordering occurs via an emergent transition that depends on interactions at both the meso- and atomic scales. In the initial experiments the transition was shown to be kinetic in nature, although a route toward true thermodynamic phase transitions was also identified. This suggests that the interplay between collective and internal energy scales could indeed open the door to phases and phase transitions that are not at present obtainable in atomic systems.

In this paper we present a simple model which captures the essence of the interplay between the meso- and the atomic length scales. The interisland interactions are allowed to influence the net moment of the elements, which provides the coupling between the length scales involved. This leaves an XY spin model with an internal degree of freedom: the spin length, which can vary with an associated energy scale. We find that, as a function of this internal energy scale, the magnetic phase transition evolves abruptly from Kosterlitz-Thouless (KT) [27] to first order at a point showing a remarkable resemblance to a tricritical point. That is, despite the absence of true long-range magnetic order and the continuously varying spin length, the phase diagram closely resembles that of the $S = 1$ Blume-Capel model [28,29]. In this case, we observe an effective critical exponent, relevant for finite-size systems, that varies continuously from that observed in 2D XY magnets of finite size, $\beta \approx 0.23$, toward a value characteristic of a tricritical point.

II. MODELING THE MAGNETIC METAMATERIAL

The total magnetic moment of interacting circular islands depends on the intrinsic material properties: internal magnetic texture, geometry, size, and separation. For instance, above the inherent ordering temperature of the material there is no magnetic order at any length scale, while below that
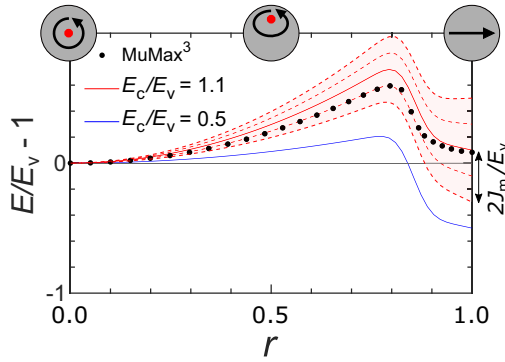
*bjorgvin.hjorvarsson@physics.uu.se

FIG. 1. The black dots represent results from micromagnetic simulations for an isolated island with $E_c/E_v \approx 1.1$. The solid (colored) lines represent the energy obtained from S [Eq. (2)] for an isolated island for two different values of E_c/E_v. The red dashed lines represent an island with four collinear neighbors when $E_c/E_v = 1.1$. Bottom dashed line: All neighbors are parallel with the island. Top dashed line: All neighbors are antiparallel. Intermediate dashed lines: Mixture of parallel and antiparallel neighbors.

temperature, both thermal fluctuations and magnetic texture on the mesoscale are essential elements dictating the moment of the islands [26]. As examples a vortex state is a magnetic texture with a zero net in-plane moment, while a collinear inner state of the islands yields the largest net moment. The single vortex state can be characterized by two observables: a continuous change of the moment within the disk and a shift of the position of the vortex core, as illustrated in the top schematic of Fig. 1. In the vortex state with a zero net moment, the vortex core sits at the center of the disk. The moment on the disk increases from zero as the vortex unwinds and approaches the disk edge. It is eventually annihilated as it moves across the edge of the magnetic island [19,22,24–26,30].

In this paper we retain the variable moment length as the main manifestation of the evolving magnetic texture, leaving the effects of the evolution in the vorticity for future work. The total moment on disk i then becomes an in-plane vector $\vec{M}_i$, allowing for the definition of an in-plane, dimensionless mesospin vector of length

$$r_i = \frac{|\vec{M}_i|}{M_{\max}}, \qquad (1)$$

where $M_{\max}$ is the magnitude of the saturated total moment. The islands can thus be viewed as mesospins whose variable length depends on the internal spin texture of the disks. It varies continuously between zero and one, depending on the competition between internal and many-body energy scales and a suitable model must include both these features.

The energy scale, E, associated with the variation of r of an isolated disk has been studied in detail in previous work [26]. The internal magnetic energy landscape of a single disk, obtained from micromagnetic simulations using MuMax^3 [31], is represented by the black dots in Fig. 1. Here we plot $E/E_v - 1$ vs r, where E_v is the energy of the pure vortex state ($r = 0$) and E_c is the energy of the collinear state ($r = 1$). The energy landscape is highly asymmetric, with a maximum at approximately $r = 0.8$, corresponding to a vortex core

positioned inside but close to the edge of the island. As the vortex core reaches the edge and moves outside the disk the energy associated with the magnetic texture rapidly decreases so that E_c lies well below the maximum energy. The ratio E_c/E_v determines whether an isolated disk carries a moment or not in its lowest energy configuration and this can be varied either side of unity by changing the disk radius [26].

As shown in the figure, the landscape is qualitatively reproduced by the following function,

$$S = E_c \left[p\left(\frac{r}{r_0}\right)^2 - p + 1 \right] + \frac{E_v}{3}(2p - r^2 + 1), \qquad (2)$$

where

$$p = \frac{1}{2}\left[1 - \mathrm{erf}\left(\frac{r - r_0}{a\sqrt{2}}\right) \right],$$

with $a = 0.035$ and $r_0 = 0.85$.

The agreement between the fitting function, $S/E_v - 1$ (solid lines), and the micromagnetic simulations (black dots) is found to be good, as seen in the figure. Also included in the figure are the effects of interdisk interactions (red dashed lines). Here the lines represent interactions of a disk with spin length r with four fully collinear neighbors ($r = 1$). The bottom dashed line represents the case when all four neighbors are parallel with the island. For each subsequent dashed line above, one neighbor has been reversed until they are all antiparallel, as represented by the top dashed line. The difference in energy is a measure of the many-body interactions that one can expect in an array of disks. Of particular interest here is the case of $E_c/E_v = 1.1$, which for the isolated disk indicates preference for a vortex state. When including interactions, however, a collinear configuration is instead favored with the mesospins lying parallel to each other. This precursor illustrates how interdisk interactions can influence the collective behavior of an array promising the emergence of rich many-body behavior.

Magnetostatic interdisk interactions can be engineered through island geometry and thickness as well as material composition to produce a wide range of symmetries, strengths, and interaction length scales [32–34]. Combining this control with variable internal properties of the disks offers access to rich possibilities for both equilibrium and nonequilibrium behavior. To illustrate this, we study the test case of a ferromagnetic interaction with continuous symmetry. With this approach, the Hamiltonian describing interactions between disks, placed on a square lattice taking into account both internal texture and many-body interactions, can be written

$$H = -J_m \sum_{\langle ij \rangle} r_i r_j \cos(\theta_i - \theta_j) + \sum_i S_i(r). \qquad (3)$$

J_m is the interaction between nearest-neighboring islands and θ is the in-plane orientation of the mesospin, $0 \leqslant \theta < 2\pi$. The first term is similar to the 2D XY model, but includes the varying spin length, $0 \leqslant r \leqslant 1$, and the second term is the parametrized r dependence defined by Eq. (2). The proposed model is similar to the vector Blume-Capel model (VBCM) [28,29,35,36] in which vector spins take discrete lengths ($r = \{0, 1\}$). The modeling of the emergent mesospin interactions

gives us, in addition, the continuous variation of r and the phenomenological energy function $S(r)$.

Anticipating the situation where, below the bulk ordering temperature, the array of interacting disks can be thermally equilibrated, or that the nonequilibrium dynamics can be well represented through an emergent effective temperature, we study the thermal properties of the proposed model. The magnetization, M, is divided up into the mesospin density R and orientation density Θ, defined

$$M = \frac{1}{L^2} \sqrt{\left(\sum_i r_i \cos\theta_i \right)^2 + \left(\sum_i r_i \sin\theta_i \right)^2},$$

$$R = \frac{1}{L^2} \sum_i r_i,$$

$$\Theta = \frac{1}{L^2} \sqrt{\left(\sum_i \cos\theta_i \right)^2 + \left(\sum_i \sin\theta_i \right)^2}. \quad (4)$$

The susceptibilities are defined by $\chi_{\mathrm{M}} = L^2 \frac{\langle M^2 \rangle - \langle M \rangle^2}{T}$, $\chi_{\mathrm{R}} = L^2 \frac{\langle R \rangle^2 - \langle R \rangle^2}{T}$, and $\chi_{\Theta} = L^2 \frac{\langle \Theta \rangle^2 - \langle \Theta \rangle^2}{T}$. Θ and χ_{Θ} correspond to the magnetization and the magnetic susceptibility of the conventional 2D XY model. It is also convenient to define the parameter $\Delta E = (E_c - E_v - 2J_m)/E_v$ whose sign designates the preference for broken symmetry or zero spin length in the lowest energy configuration. The parameter ΔE could be controlled experimentally by varying disk radius, thickness, form, and separation. In this paper we report results with the fixed ratio $J_m = 0.2E_v$, so that the degeneracy between the vacuum state and the fully ordered magnetic state for the disks is obtained when $\Delta E = -0.4$, which marks a point of major importance in this work.

III. METHODS

Arrays of L^2 mesospins on a square lattice with periodic boundaries were simulated using the Metropolis algorithm. $L = 32$ unless otherwise stated. Each calculation was based upon 40 000 thermalization full lattice sweeps prior to 400 000 measurement sweeps, to ensure thermal equilibration and statistically robust results [37,38]. A full lattice sweep entails attempting to update both r and θ once for each lattice site. The required thermalization timescales were established through monitoring the relaxation timescale for M. E_c/E_v was varied while always keeping $J_m = 0.2E_v$. The initial state at each temperature was set to either a random spin configuration with respect to both θ and r in a "hot start" or an ordered, fully magnetized configuration in a "cold start."

IV. RESULTS

The magnetization, M, obtained from simulation is shown in Fig. 2 for different ΔE values from a hot start. The results reveal transitions from a high-temperature disordered phase to a low-temperature quasiordered phase. For negative values of ΔE, a ferromagnetic ground state is energetically favorable. For ΔE large and negative the transitions are smooth, with the
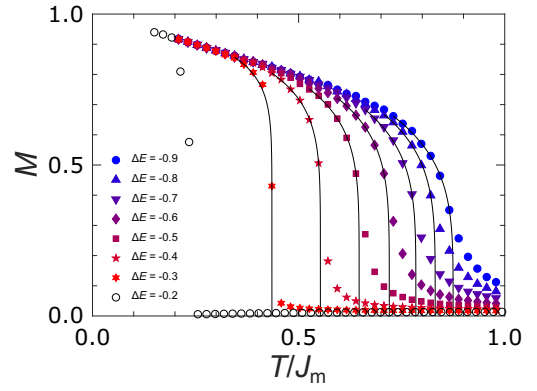

FIG. 2. Transitions for different values of ΔE. The transition becomes sharper with increasing ΔE, and becoming discontinuous for $\Delta E = -0.2$.

finite-size magnetization resembling that observed through the KT transition of the 2D XY model, or plane rotator model [39,40]. Increasing ΔE causes a sharpening of the transition, up to an apparent tricritical point with $\Delta E \approx -0.3$. Increasing beyond this value, the finite-size magnetization undergoes a discontinuous jump, as in a first-order transition; see for example $\Delta E = -0.2$. For higher values ($\Delta E \geqslant -0.1$), the transition into an ordered collinear phase does not occur.

The curves in Fig. 2 are fits to the data sets of the form $M = M_0(T - T_c)^{\beta}$, where T_c and β are free parameters and $M_0 = 1$. Given this phenomenology, one should perhaps consider these curves as guides to the eye, although for ΔE large and negative the results are consistent with the zero parameter fitting procedure outlined in Ref. [39] as well as with many experimental observations [41]. However, rather provocatively, the observed effective exponent β does evolve in a way that is perfectly compatible with observations in a finite system as it crosses over from critical to tricritical behavior. The best-fit exponents for a few values of ΔE are shown in the upper panel of Fig. 3. Starting from the expected value for the finite 2D XY model for $\Delta E < -0.9$, the fitted β decreases continuously to less than half its initial value, with $\beta \approx 0.1$ close to the apparent tricritical point. This evolution should be compared with mean-field theory where the tricritical exponent $\beta_{\mathrm{tri}} = 1/4$, down from $\beta = 1/2$ at the regular critical point, and with the 2D Blume-Capel model where $\beta_{\mathrm{tri}} = 1/24$ [42] is only one-third of the 2D Ising critical exponent $\beta = 1/8$. We note that the effective tricritical exponent is quite close to the critical exponent for the Ising model, $\beta = 1/8$, although it is difficult to incorporate this observation into a tricritical scenario for quasiordering of the rotors.

In the lower panel of Fig. 3 we show the evolution of the transition temperature as ΔE increases. For $\Delta E < -0.9$, T_{C} slightly overshoots the extrapolated transition temperature value for the plane rotator model $T_{\mathrm{C}} \approx 0.898J_m$ [43]. The overshoot is consistent with the expected logarithmic shift in the effective transition temperature with system size [39]. T_{C} then decreases with increasing ΔE reaching approximately half the plane rotator transition temperature at the tricritical point before dropping discontinuously to zero for ΔE between -0.3 and -0.2.
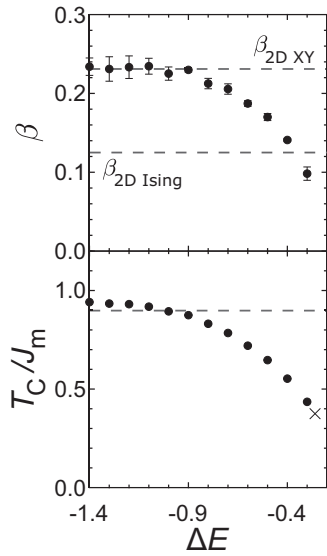
FIG. 3. Top panel: The effective critical exponent β as a function of ΔE. The upper dashed line shows $\beta = 0.231$, the effective exponent of the 2D XY model. The lower dashed line shows $\beta = 1/8$, the value for the 2D Ising model. Bottom panel: The finite-size ordering temperature, T_C. The dashed line shows $T_{KT} = 0.898 J_{\mathrm{m}}$, the extrapolated value for the 2D XY model. The cross marks the estimated tricritical temperature.

The continuous evolution of a measured critical exponent from the critical to the tricritical value as tricriticality is approached is a crossover effect depending on corrections to the scaling of the asymptotic regime. That is, the tricritical fixed point of a renormalization group flow is unstable to approach from any direction. As a consequence, flows from any point on the order-disorder phase boundary will take the system back toward the critical fixed point [44]. This crossover effect is controlled by a crossover exponent ϕ, giving a characteristic crossover length scale which diverges as the tricritical point is approached. As a result, there is a continuous evolution of the measured exponent (in this case the order parameter exponent β) for fixed system size, as one enters the tricritical region. At a fixed distance from the tricritical point, one can therefore expect an evolution of this exponent with system size, back toward its critical value.

For our system, as the order parameter exponent for the BKT transition is itself an effective exponent, the finite-size scaling is at present an open field of study. We have repeated the approach to tricriticality for system sizes $L = 16$ and $L = 64$ in addition to those for $L = 32$ presented above. In Fig. 4 we show the evolution of the effective exponent β with $\frac{1}{L}$ for $\Delta E = -0.7$ and $\Delta E = -0.4$. In each case, there is evolution of the exponent to higher values as $\frac{1}{L}$ decreases. For $\Delta E = -0.7$ the effective exponent extrapolates rather spectacularly to $\beta \approx 0.23$ as $\frac{1}{L} \to 0$ suggesting a crossover exponent ϕ close to unity. However, this scaling is not repeated closer to the tricritical point. For $\Delta E = -0.4$, with some caution, we can again report linear scaling with $\frac{1}{L}$, but the extrapolated value falls well below 0.23. More detailed and extensive studies are required but our results already raise
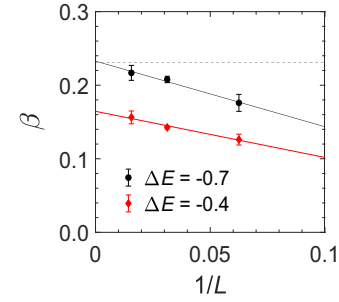

FIG. 4. Evolution of effective critical exponent β with inverse system size, $\frac{1}{L}$. Full lines show linear fits and the dashed line shows $\beta = 0.231$.

the prospect of rich behavior, falling outside the confines of critical finite-size scaling.

Figure 5 shows our estimation of the transition temperature over the same range of system sizes. In both cases a small evolution is observed toward lower temperatures for larger system sizes. In Kosterlitz-Thouless systems, the effective transition temperature, corresponding to that at which the correlation length equals the system size [39,45,46], should scale logarithmically with L,

$$T_C(L) - T_{KT}^{\Delta E} = \frac{\pi^2}{c(\ln L)^2}. \tag{5}$$

Our data for both $\Delta E = -0.7$ and $\Delta E = -0.4$ are consistent with this, as shown in Fig. 5, although away from the $\Delta E \to -\infty$ limit $T_{KT}^{\Delta E}$ is not known so that Eq. (5) has two fitting parameters.

The change in the nature of the transition from KT to first order is driven by the change in rotor length, as shown in the upper panel of Fig. 6, where we plot R vs T for different ΔE values. As ΔE passes through $-2J_{\mathrm{m}} = -0.4$ the role played in the free energy by the rotor length changes. For $\Delta E < -0.4$, placing a rotor of maximum length leads to a gain in internal energy for both random and correlated spin configurations. As a consequence, the internal energy favors an ordered state with $R = 1$, while entropic forces drive R below unity, with maximum entropy for $R = 0.5$. For ΔE considerably greater than -0.4, energy costs are such that $R \to 0$ as $T \to 0$ so that entropy drives the growth in R at all finite temperatures. Between these two limits there is a small window of ΔE for which finite R is energetically favorable if
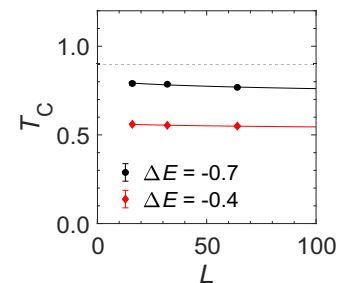

FIG. 5. Evolution of fitted transition temperature with system size: $\Delta E = -0.7$, black dots; $\Delta E = -0.4$, red dots. Full lines show fits to Eq. (5) and the dashed line shows $T_{KT} = 0.898 J_m$.
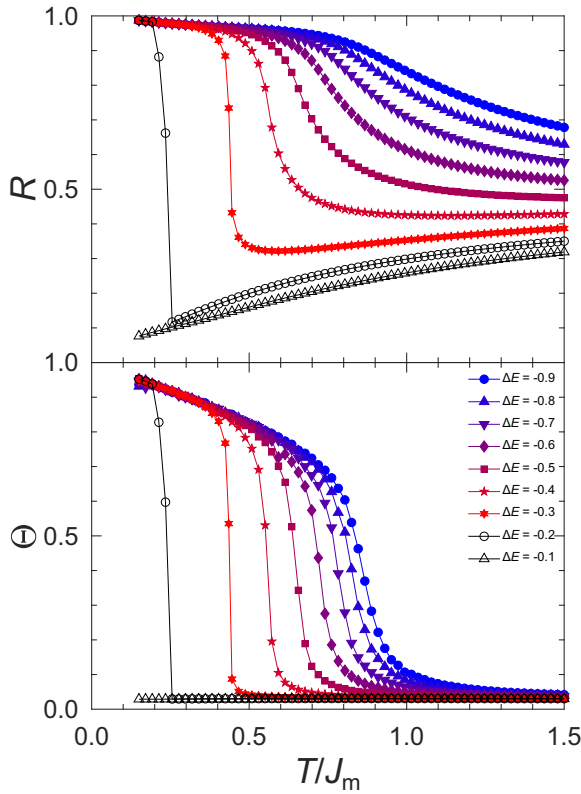
FIG. 6. Top panel: The average mesospin length R vs temperature for different ΔE. Bottom panel: The orientation density Θ vs temperature for different ΔE. The open symbols indicate values of ΔE in the first-order region of the phase diagram.

symmetry is broken (or almost broken in the case of a KT transition); otherwise it is entropically driven and energetically unfavourable. This phenomenology is well illustrated in Fig. 6 which shows R to be a monotonically increasing function as temperature is reduced for $\Delta E < -0.6$. For greater values of ΔE, R dips below 0.5 and for $\Delta E = -0.3$, the approximate tricritical value R clearly decreases as T falls to intermediate values before rebounding to large values through the phase transition. It is this "elastic" resistance to large R values at low temperature that drives the transition first order. At $\Delta E = -0.2$ the transition is clearly first order, while for $\Delta E = -0.1$ no symmetry breaking is observed and R decreases monotonically to zero as $T \to 0$.

This phenomenology in which energy gain at large R depends explicitly on symmetry breaking is generic to tricritical systems. Similar behavior is observed for the VBCM in two dimensions (see Appendix) and in systems with discrete symmetry [47]. However, there are effects specific to the model studied here which allows for continuous variation of the rotor length. Close examination of Fig. 6 shows that R drops below 0.5 at intermediate temperature, even for $\Delta E = -0.5$ and $\Delta E = -0.4$, while in the equivalent figure for the VBCM (see Appendix), R remains greater than 0.5 for all $\Delta E \leqslant -0.4$. This difference arises as the system profits from the entropy associated with a continuous spread of rotor lengths, despite the energy gain from placing rotors of fixed length $r = 1$. This

is clearly a nonuniversal effect depending on the form of $S(r)$ and could be modified in different nanoengineered arrays.

The KT transition is, from a thermodynamic point of view, extremely special as there is no true magnetic symmetry breaking and so no order parameter in the thermodynamic sense. At first sight this might suggest that a first-order transition signaled by a discontinuous jump in such a parameter should be excluded. However, the day is saved here by the parameter R, which is a scalar measure of the mesospin density and which is a well defined intensive thermodynamic variable at all temperatures. A thermodynamic signal of the first-order transition is therefore a discontinuous jump in R. However, the spin density remains coupled to the magnetization and to the development of quasi-long-range orientational order for the mesospins through the tricritical point and into the first-order regime. This is illustrated in the lower panel of Fig. 6, where we show the evolution of Θ with temperature for different values of ΔE. The purely orientation order parameter mimics M, with the pseudocritical range narrowing as the tricritical point is approached.

The development of tricritical coupling between spin density and spin rotation degrees of freedom is illustrated by the three susceptibilities shown in Fig. 7. For $\Delta E < -0.6$, which is deep in the Kosterlitz-Thouless region, χ_M and χ_Θ show a finite-size rounded divergence at the same temperature, which can be fitted to the characteristic exponential form for the KT transition (not shown), while χ_R shows a rounded maximum at temperatures that are decoupled from the KT transition and two orders of magnitude smaller than the singular susceptibilities. As ΔE increases into the crossover region toward tricriticality, a sharp peak in χ_R emerges. It rapidly locks onto the divergences in χ_M and χ_Θ which also sharpen so that, on arriving at the apparent tricritical point, the three susceptibilities show the same sharply singular feature. This can be taken as a signature of the coupling of the internal and external degrees of freedom of the mesospins.

Within the first-order regime, the three regions—the high-temperature entropic regime, the unfavorable intermediate-temperature regime, and the broken-symmetry ordered phase—are illustrated in Fig. 8 in the upper panel. The figure shows snapshots for different temperatures, for $\Delta E = -0.2$. As we are in the regime where, in the absence of interactions, the vortex state is favored, the low-energy magnetic state is generated through many-body interactions. In region III both orientational disorder and a wide range of rotor lengths can be observed. In region II while the rotors remain disordered their mean length is clearly reduced, reflecting the energy cost of creating full length rotors while remaining in the disordered phase. In the low-temperature phase, I, the symmetry breaking allows for an energy gain on generating extended rotors. In the lower panel we show χ_R on a linear scale over the same temperature range. Entry into the intermediate range is marked by a broad maximum at around $T = 0.5J_m$ signaling a rapid reduction in mean rotor length. Below this point, χ_R decreases until it hits the first-order discontinuity at $T \approx 0.25J_m$ below which the rotor length remains more or less fixed near the maximum value. Also shown is the rotor susceptibility for a noninteracting system ($J_m = 0$). The peak at intermediate temperature is lower and broader when interactions are switched off, illustrating that rotor-rotor
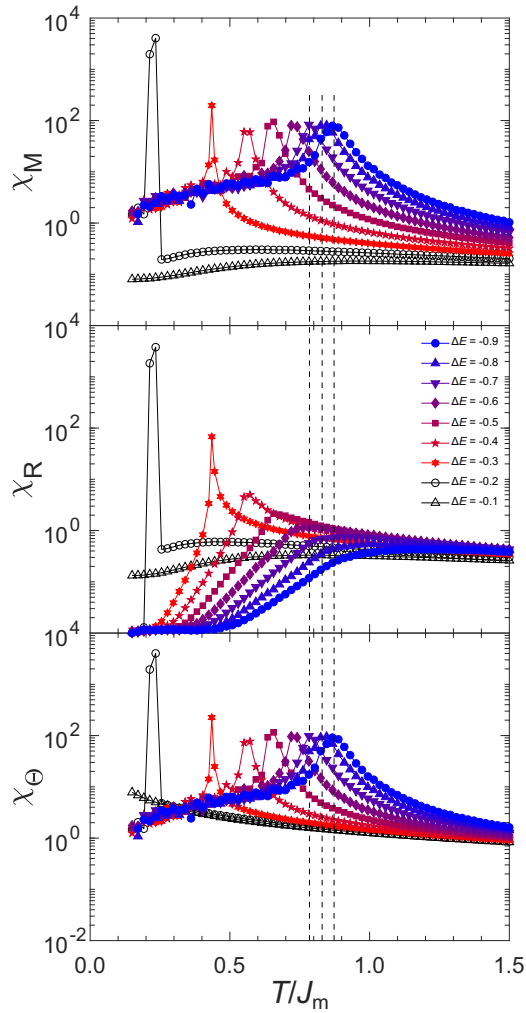
FIG. 7. Susceptibility vs temperature for different ΔE. Top panel: The magnetic susceptibility χ_M. Middle panel: The mesospin density susceptibility χ_R. Bottom panel: The orientation density susceptibility χ_Θ. The vertical dotted lines show the peak positions overlapping in χ_M and χ_Θ, but not in χ_R, for the three lowest values of ΔE.

interactions offset the energy cost of finite spin length, helping to maintain their presence down to lower temperatures.

The data shown in Figs. 2, 6, and 7 are for hot starts for fixed ΔE. Following this protocol, the symmetry-breaking transition disappears between $\Delta E = -0.2$ and -0.1 even though the ground state of an ordered configuration with rotors of unit length remains lower than any disordered state for $\Delta E < 0$. The loss of the transition in this range is a nonequilibrium result characteristic of a first-order transition and the presence of metastable states. Making runs from cold starts exposes hysteresis in M, due to the loss of ergodicity as shown in Fig. 9. For $\Delta E = -0.1$ the ordered state survives a cold start up to $T = 0.15 J_m$ and the metastability survives up to around $\Delta E = -0.3$ in the tricritical region.

The hysteresis can also be observed by ramping ΔE in loops from negative values upward and back again, while holding the temperature fixed [38]. The full phase diagram in the $\Delta E, T$ plane from loops ramping ΔE at fixed temperature
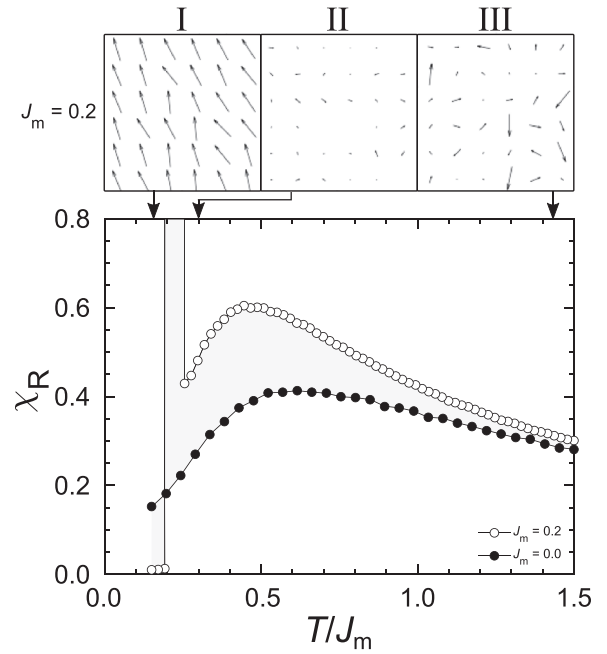

FIG. 8. Upper panel: Snapshots of mesospin configurations at high (III), intermediate (II), and low temperatures (I). In (III) a full range of r values is observed, while in (II) the range is limited to small values. Transformation from (III) to (II) is a crossover. Evolution from (II) to (I) is via a first-order transition for $J_m \neq 0$. Lower panel: χ_R as a function of temperature for $\Delta E = -0.2$, with and without interactions.

is shown in Fig. 10. This phase diagram is similar to that observed for the VBCM [38]. The ordered phase resists finite-temperature fluctuations up to $\Delta E \approx 0.3$, considerably above the equilibrium threshold for stability of the ordered phase. The figure therefore shows a finite region of metastability in which the ordered and disordered phases, labeled I and II, coexist for simulations of fixed timescale. The zone of metastability closes at the tricritical point and ramping ΔE gives an alternative measure of its position, which we estimate to be $\Delta E = -0.26 \pm 0.01$, $T_{tri} = 0.375 \pm 0.025$. This is in good qualitative agreement with our estimate from the evolution of the effective critical exponent. The true phase
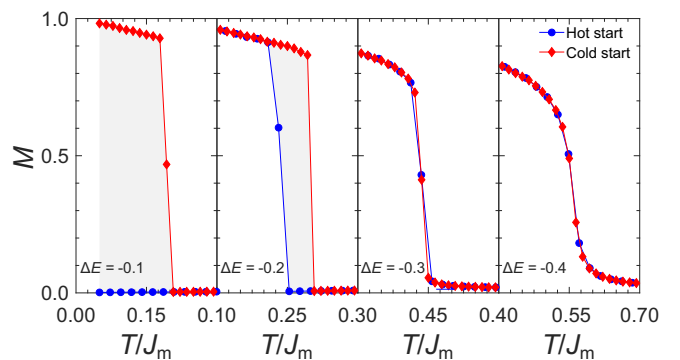

FIG. 9. M as a function of temperature for different values of ΔE, starting at random (hot start) or collinear (cold start) spin configurations at each temperature.
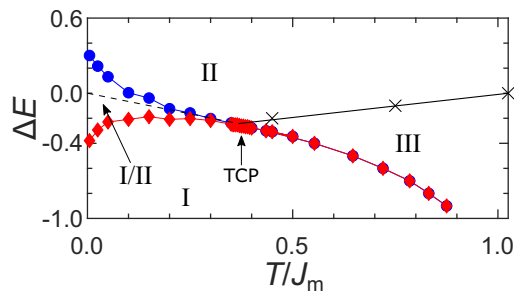
FIG. 10. The phase diagram showing the tricritical point (TCP) separating the first- and second-order behavior. The dashed line represents the phase boundary in region of first-order transitions and the area between blue (cold start) and red (hot start) points marks the region of metastability. The three X's indicate the positions of the broad maximum in χ_R (shown in Fig. 8 for $\Delta E = -0.2$) for $\Delta E = \{-0.2, -0.1, 0.0\}$. The solid line connecting the crosses is a guide to the eye.

boundary must run close to the line extrapolating between $\Delta E = 0$ at $T = 0$ and the tricritical point, as shown in Fig. 10, although we have not attempted to evaluate it in detail. The crossover between regions II and III in which the rotors are confined to short lengths and in which a full spread of lengths appear is also shown. The position of the broad maximum in χ_R which characterizes the crossover is marked for $\Delta E = \{-0.2, -0.1, 0.0\}$.

V. DISCUSSION

We have shown that engineered two-dimensional arrays of magnetic disks on the mesoscale offer interactions that map convincingly onto a model system showing tricriticality. In this development, we represent interdisk interactions and internal spin textures by an effective nearest-neighbor coupling between magnetic mesospins of varying length. The energy scale fixing the mesospin length is the magnetic vortex core energy, giving a Blume-Capel type model [28,29] with both continuous, in-plane rotor orientations [38,48] and continuous rotor length. The tricriticality observed numerically is rather special in that it marks the evolution from a Kosterlitz-Thouless phase transition to a first-order transition [38,48,49].

Tricritical systems are the confluence of three phases whose thermodynamics is governed by three independent
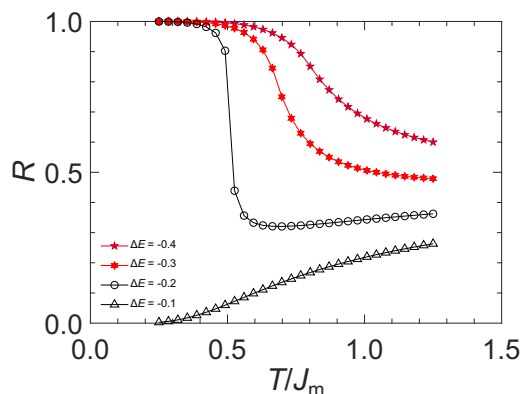
thermodynamic variables [50]. As a consequence their critical properties are characterized by three scaling variables [51] and associated critical exponents [44]. This situation is captured most simply by the Blume-Capel model (BCM) [28,29], in which temperature and field conjugate to an order parameter with Z_2 symmetry are joined by an energy scale or chemical potential associated with spin creation and annihilation.

Archetypal examples of tricritical systems are the merger of the superfluid transition of ^{4}He and the critical point of the demixing transition in ^{4}He $- ^3$He mixtures [52,53], or the smectic-C^*–smectic-A transition, which evolves through tricriticality on mixing two species of liquid crystal [54]. Experimental studies of the tricriticality are complicated by the difficulty in accessing the three intensive thermodynamic variables. For example for ^{4}He $- ^3$He mixtures, while exquisite temperature control is possible [55], the field conjugate to the superconducting order parameter is inaccessible. The mixture can be controlled by varying the ^{3}He mole fraction which serves as a second-order parameter, but the true intensive variable, the chemical potential difference $\mu = \mu_{^3\text{He}} - \mu_{^4\text{He}}$, is also inaccessible. In principle, μ could be controlled in ultrathin helium films [56] but the experimental environment is extremely challenging. In other systems, the situation is even more constrained. Arrays of Josephson junctions can be diluted [57], allowing the approach to tricriticality, but the procedure introduces quenched site disorder and the complexity associated with it. First-order magnetic transitions occur, for example, in FeRh films [58] or in spin ice materials [59]. These transitions could be tuned to tricriticality [60,61], but this would require control of both the coupling constant and the chemical potential through applied pressure or site dilution.

The magnetization of a system of finite size is a prime experimental indicator of the Kosterliz-Thouless phase transition [39]. It changes in a characteristic manner though the transition, with the emergence of an effective magnetic critical exponent $\beta \approx 0.23$ [41]. We have shown here that the effective magnetization exponent crosses over toward tricriticality in an analogous manner to a thermodynamic exponent, with an effective tricritical value less than half the critical value, as is the case for the two-dimensional BCM [42,62]. Going beyond this phenomenology would require more extensive numerics and a deeper examination of the theory. This paper provides a platform for this in future work, but more importantly for the present, this straightforward approach provides a platform for experiments on arrays of mesoscale disks in which order parameter crossover, effective or otherwise, should be accessible to measurement.

In such experiments all three intensive thermodynamic variables relative to the tricritical phase diagram can be controlled through the change of disk spacing, radius, and thickness [26] and application of an external field. Further, system size will be an independent control parameter of these metamagnetic systems, providing experimental access to finite-size scaling. This is a powerful tool for simulation [62], but is generally outside the realm of experiment in condensed matter systems. Artificial systems such as the mesospin arrays presented here or cold atom platforms [63] could provide future access to this essential phenomenology.

FIG. 11. Results from the discretized model where $r = \{0, 1\}$.

Experimental arrays on a square lattice would most likely retain anisotropic interactions, in which case we anticipate a return to the original BCM model with a tricritical point and critical behavior in the Ising universality class. Model systems order antiferromagnetically [64] but disk arrays can order differently, with chain formation [7,33,65], while lifting of the cubic symmetry could lead to ferromagnetic states, as is the case for their three-dimensional counterparts [66]. Continuous symmetry could emerge in triangular arrays [64,67] and experimental systems can be ferromagnetic [33] so that nanoarray tricriticality, a Kosterlitz-Thouless phase transition, and even ferromagnetism, as reported here, are all experimental possibilities. The triangular system is potentially doubly rich, as it offers two Kosterlitz-Thouless phase transitions [67] delimiting the phase with emergent continuous symmetry. The fate of this phase in the presence of variable spin length is an interesting problem, pertinent for the long-standing problem of two-dimensional melting [68–70].

BCM and vector-BCM (VBCM) models have been further extended to Blume-Emergy-Griffiths (BEGM) type models [35,36,44,71] to describe the full $^4\mathrm{He} - ^3\mathrm{He}$ phase diagram. Here, a biquadratic interaction between spins is added capturing isotropic interactions. The extra term introduces the possibility of separating the demixing from the ordering of the internal degree of freedom, allowing for liquid-gas-like criticality, $^4\mathrm{He} - ^3\mathrm{He}$ tricriticality, and a triple point between superfluid, normal $^4\mathrm{He}$-rich and $^3\mathrm{He}$-rich phases in both three [35] and two dimensions [48,49,72]. The extra biquadratic term could also be engineered in the nanoarrays by modification of the disk topology, leading to the development of quadrupole interactions. This would allow for the experimental study of models resembling the BEGM and vector-BEGM in two dimensions.

VI. CONCLUSION

The experimental realization of emergent tricriticality in magnetic metamaterials with coupled intra- and interisland excitations poses serious experimental challenges, notably the creation of an environment showing equilibrium thermodynamics (real or effective) and controlled departures from it. However it offers a test case that prepares the ground for a vast array of possibilities offered by nanoengineered metamagnets, with both fundamental exploration and technological applications in mind. In particular, the identification of mesospins of variable length in controlled out-of-equilibrium environments invites applications in adaptive matter [73] through the dynamical modification of the many-body energy landscape [74]. The self-modification of the energy discussed

here is analogous to the interstitial self-trapping of hydrogen in metals, where the hydrogen interstitial and the local strain field form a dynamic quasiparticle [75]. Local energy landscape fluctuations within an array of mesospins could also offer local sensing capabilities and long-term memory, a further cornerstone of adaptive or intelligent matter [73]. Clever engineering of the metamaterials may therefore offer pathways toward more advanced materials or even analog logic mesospin components [76].

All data are available from the corresponding author upon reasonable request.

APPENDIX

In the context of our work, the Hamiltonian for the VBCM is defined

$$H = -J_\mathrm{m} \sum_{\langle ij \rangle} r_i r_j \cos(\theta_i - \theta_j) + \sum_i D r_i, \qquad \text{(A1)}$$

with $D = E_\mathrm{c} - E_\mathrm{v}$. The spin length r_i now takes on one of two values: $r_i = 1$ or $r_i = \epsilon$, $\lim \epsilon \to 0$. Taking the limit $r_i \to 0$ attributes a phantom rotational degree of freedom to the vacancy, ensuring that it occupies the same volume in configuration space as a site filled with a classical spin. With this precaution the integrals of the partition function can be normalized by 2π [36], so that $R \to 0.5$ at high temperature. As before, the dimensionless energy shift is defined $\Delta E = (D - 2J_\mathrm{m})/E_\mathrm{v}$.

The evolution of R vs temperature for different ΔE values is shown in Fig. 11 confirming the predicted behavior at high temperature. For $\Delta E \leqslant -0.4$, R remains greater than 0.5 over the whole temperature range. This is in contrast with the model in the main text with continuous variation in r_i, in which R dips below 0.5 at intermediate temperatures for both $\Delta E = -0.4$ and $\Delta E = -0.5$.

[1] V. Kapaklis, U. B. Arnalds, A. Harman-Clarke, E. T. Papaioannou, M. Karimipour, P. Korelis, A. Taroni, P. C. W. Holdsworth, S. T. Bramwell, and B. Hjörvarsson, Melting artificial spin ice, New J. Phys. **14**, 035009 (2012).

[2] O. Sendetskyi, V. Scagnoli, N. Leo, L. Anghinolfi, A. Alberca, J. Lüning, U. Staub, P. M. Derlet, and L. J. Heyderman,

Continuous magnetic phase transition in artificial square ice, Phys. Rev. B **99**, 214430 (2019).

[3] E. Östman, U. B. Arnalds, V. Kapaklis, A. Taroni, and B. Hjörvarsson, Ising-like behaviour of mesoscopic magnetic chains, J. Phys.: Condens. Matter **30**, 365301 (2018).

[4] U. B. Arnalds, M. Ahlberg, M. S. Brewer, V. Kapaklis, E. T. Papaioannou, M. Karimipour, P. Korelis, A. Stein, S. Ólafsson,

T. P. A. Hase, and B. Hjörvarsson, Thermal transitions in nano-patterned XY-magnets, Appl. Phys. Lett. **105**, 042409 (2014).

[5] C. Nisoli, R. Moessner, and P. Schiffer, Colloquium: Artificial spin ice: Designing and imaging magnetic frustration, Rev. Mod. Phys. **85**, 1473 (2013).

[6] C. Nisoli, V. Kapaklis, and P. Schiffer, Deliberate exotic magnetism via frustration and topology, Nat. Phys. **13**, 200 (2017).

[7] M. Ewerlin, D. Demirbas, F. Brüssing, O. Petracic, A. A. Ünal, S. Valencia, F. Kronast, and H. Zabel, Magnetic Dipole and Higher Pole Interaction on a Square Lattice, Phys. Rev. Lett. **110**, 177209 (2013).

[8] N. Leo, S. Holenstein, D. Schildknecht, O. Sendetskyi, H. Luetkens, P. M. Derlet, V. Scagnoli, D. Lançon, J. R. L. Mardegan, T. Prokscha, A. Suter, Z. Salman, S. Lee, and L. J. Heyderman, Collective magnetism in an artificial 2D XY spin system, Nat. Commun. **9**, 2850 (2018).

[9] U. B. Arnalds, J. Chico, H. Stopfel, V. Kapaklis, O. Bärenbold, M. A. Verschuuren, U. Wolff, V. Neu, A. Bergman, and B. Hjörvarsson, A new look on the two-dimensional ising model: Thermal artificial spins, New J. Phys. **18**, 023008 (2016).

[10] R. Streubel, N. Kent, S. Dhuey, A. Scholl, S. Kevan, and P. Fischer, Spatial and temporal correlations of *XY* macro spins, Nano Lett. **18**, 7428 (2018).

[11] R. F. Wang, C. Nisoli, R. S. Freitas, J. Li, W. McConville, B. J. Cooley, M. S. Lund, N. Samarth, C. Leighton, V. H. Crespi, and P. Schiffer, Artificial "spin ice" in a geometrically frustrated lattice of nanoscale ferromagnetic islands, Nature (London) **439**, 303 (2006).

[12] A. Farhan, P. Derlet, A. Kleibert, A. Balan, R. Chopdekar, M. Wyss, L. Anghinolfi, F. Nolting, and L. J. Heyderman, Exploring hyper-cubic energy landscapes in thermally active finite artificial spin-ice systems, Nat. Phys. **9**, 375 (2013).

[13] S. Ladak, D. E. Read, G. K. Perkins, L. F. Cohen, and W. R. Branford, Direct observation of magnetic monopole defects in an artificial spin-ice system, Nat. Phys. **6**, 359 (2010).

[14] A. Farhan, P. M. Derlet, A. Kleibert, A. Balan, R. V. Chopdekar, M. Wyss, J. Perron, A. Scholl, F. Nolting, and L. J. Heyderman, Direct Observation of Thermal Relaxation in Artificial Spin Ice, Phys. Rev. Lett. **111**, 057204 (2013).

[15] V. Kapaklis, U. B. Arnalds, A. Farhan, R. V. Chopdekar, A. Balan, A. Scholl, L. J. Heyderman, and B. Hjörvarsson, Thermal fluctuations in artificial spin ice, Nat. Nanotechnol. **9**, 514 (2014).

[16] J. P. Morgan, A. Stein, S. Langridge, and C. H. Marrows, Thermal ground-state ordering and elementary excitations in artificial magnetic square ice, Nat. Phys. **7**, 75 (2011).

[17] Y. Qi, T. Brintlinger, and J. Cumings, Direct observation of the ice rule in an artificial kagome spin ice, Phys. Rev. B **77**, 094418 (2008).

[18] J. P. Morgan, J. Akerman, A. Stein, C. Phatak, R. M. L. Evans, S. Langridge, and C. H. Marrows, Real and effective thermal equilibrium in artificial square spin ices, Phys. Rev. B **87**, 024405 (2013).

[19] R. P. Cowburn, D. K. Koltsov, A. O. Adeyeye, M. E. Welland, and D. M. Tricker, Single-Domain Circular Nanomagnets, Phys. Rev. Lett. **83**, 1042 (1999).

[20] S. D. Slöetjes, B. Hjörvarsson, and V. Kapaklis, The effect of confinement on thermal fluctuations in nanomagnets, Appl. Phys. Lett. **118**, 142407 (2021).

[21] S. Gliga, A. Kákay, L. J. Heyderman, R. Hertel, and O. G. Heinonen, Broken vertex symmetry and finite zero-point entropy in the artificial square ice ground state, Phys. Rev. B **92**, 060413(R) (2015).

[22] T. Shinjo, Magnetic vortex core observation in circular dots of permalloy, Science **289**, 930 (2000).

[23] M. Kläui, C. A. F. Vaz, L. Lopez-Diaz, and J. A. C. Bland, Vortex formation in narrow ferromagnetic rings, J. Phys.: Condens. Matter **15**, R985 (2003).

[24] H. F. Ding, A. K. Schmid, D. Li, K. Y. Guslienko, and S. D. Bader, Magnetic Bistability of Co Nanodots, Phys. Rev. Lett. **94**, 157202 (2005).

[25] E. Östman, U. B. Arnalds, E. Melander, V. Kapaklis, G. K. Pálsson, A. Y. Saw, M. A. Verschuuren, F. Kronast, E. T. Papaioannou, C. S. Fadley, and B. Hjörvarsson, Hysteresis-free switching between vortex and collinear magnetic states, New J. Phys. **16**, 053002 (2014).

[26] B. E. Skovdal, N. Strandqvist, H. Stopfel, M. Pohlit, T. Warnatz, S. D. Slöetjes, V. Kapaklis, and B. Hjörvarsson, Temperature-induced collapse of spin dimensionality in magnetic metamaterials, Phys. Rev. B **104**, 014434 (2021).

[27] J. M. Kosterlitz and D. J. Thouless, Ordering, metastability and phase transitions in two-dimensional systems, J. Phys. C: Solid State Phys. **6**, 1181 (1973).

[28] M. Blume, Theory of the first-order magnetic phase change in UO_2, Phys. Rev. **141**, 517 (1966).

[29] H. Capel, On the possibility of first-order phase transitions in Ising systems of triplet ions with zero-field splitting, Physica **32**, 966 (1966).

[30] O. Tchernyshyov and G.-W. Chern, Fractional Vortices and Composite Domain Walls in Flat Nanomagnets, Phys. Rev. Lett. **95**, 197204 (2005).

[31] A. Vansteenkiste, J. Leliaert, M. Dvornik, M. Helsen, F. Garcia-Sanchez, and B. Van Waeyenberge, The design and verification of MuMax3, AIP Adv. **4**, 107133 (2014).

[32] S. D. Slöetjes, H. H. Urdahl, J. K. Grepstad, and E. Folven, Tailoring the magnetic order in a supermagnetic metamaterial, AIP Adv. **7**, 056325 (2017).

[33] E. Digernes, S. D. Slöetjes, A. Strømberg, A. D. Bang, F. K. Olsen, E. Arenholz, R. V. Chopdekar, J. K. Grepstad, and E. Folven, Direct imaging of long-range ferromagnetic and anti-ferromagnetic order in a dipolar metamaterial, Phys. Rev. Res. **2**, 013222 (2020).

[34] S. D. Slöetjes, E. S. Digernes, A. Strømberg, F. K. Olsen, A. D. Bang, A. T. N'Diaye, R. V. Chopdekar, E. Folven, and J. K. Grepstad, Effects of array shape and disk ellipticity in dipolar-coupled magnetic metamaterials, Phys. Rev. B **104**, 134421 (2021).

[35] A. Maciołek, M. Krech, and S. Dietrich, Phase diagram of a model for ^3He-^4He mixtures in three dimensions, Phys. Rev. E **69**, 036117 (2004).

[36] A. N. Berker and D. R. Nelson, Superfluidity and phase separation in helium films, Phys. Rev. B **19**, 2488 (1979).

[37] J. F. Fernández, M. F. Ferreira, and J. Stankiewicz, Critical behavior of the two-dimensional XY model: A Monte Carlo simulation, Phys. Rev. B **34**, 292 (1986).

[38] B. S. Dillon, S. Chiesa, and R. T. Scalettar, Monte Carlo study of the two-dimensional vector Blume-Capel model, Phys. Rev. B **82**, 184421 (2010).

[39] S. Bramwell and P. Holdsworth, Magnetization and universal sub-critical behaviour in two-dimensional XY magnets, J. Phys.: Condens. Matter **5**, L53 (1993).

[40] S. T. Bramwell and P. C. W. Holdsworth, Magnetization: A characteristic of the Kosterlitz-Thouless-Berezinskii transition, Phys. Rev. B **49**, 8811 (1994).

[41] A. Taroni, S. T. Bramwell, and P. C. W. Holdsworth, Universal window for two-dimensional critical exponents, J. Phys.: Condens. Matter **20**, 275233 (2008).

[42] S. Ejima, F. Lange, F. H. L. Essler, and H. A. Fehske, Critical behavior of the extended Hubbard model with bond dimerization, Phys. B: Condens. Matter **536**, 474 (2018).

[43] R. Gupta, J. DeLapp, G. G. Batrouni, G. C. Fox, C. F. Baillie, and J. Apostolakis, Phase Transition in the 2DXY Model, Phys. Rev. Lett. **61**, 1996 (1988).

[44] J. Cardy, *Scaling and Renormalization in Statistical Physics*, 1st ed., Cambridge Lecture Notes in Physics, Vol. 5 (Cambridge University Press, Cambridge, 1996).

[45] D. Venus, Renormalization group analysis of the finite two-dimensional XY model with fourfold anisotropy: Application to the magnetic susceptibility of a ferromagnetic ultrathin film, Phys. Rev. B **105**, 235440 (2022).

[46] G. A. Silva, J. A. Plascak, and D. P. Landau, Incommensurate phases in the two-dimensional *XY* model with Dzyaloshinskii-Moriya interactions, Phys. Rev. E **106**, 044116 (2022).

[47] M. E. Brooks-Bartlett, S. T. Banks, L. D. C. Jaubert, A. Harman-Clarke, and P. C. W. Holdsworth, Magnetic-Moment Fragmentation and Monopole Crystallization, Phys. Rev. X **4**, 011007 (2014).

[48] H. Chamati and S. Romano, First-order phase transitions in classical lattice gas spin models, Phys. Rev. B **75**, 184413 (2007).

[49] J. B. Santos-Filho, J. A. Plascak, M. C. Sobrinho, and T. S. A. Araujo Batista, Phase diagram of the XY vector Blume-Emery-Griffiths model on a kagome lattice by Monte Carlo simulation, Physica A **503**, 844 (2018).

[50] R. B. Griffiths, Thermodynamics Near the Two-Fluid Critical Mixing Point in He^3−He^4, Phys. Rev. Lett. **24**, 715 (1970).

[51] E. K. Riedel, Scaling Approach to Tricritical Phase Transitions, Phys. Rev. Lett. **28**, 675 (1972).

[52] E. H. Graf, D. M. Lee, and J. D. Reppy, Phase Separation and the Superfluid Transition in Liquid He^3−He^4 Mixtures, Phys. Rev. Lett. **19**, 417 (1967).

[53] R. Garcia and M. H. W. Chan, Critical Casimir Effect Near the ^{3}He - ^{4}He Tricritical Point, Phys. Rev. Lett. **88**, 086101 (2002).

[54] R. Shashidhar, B. R. Ratna, G. G. Nair, S. K. Prasad, C. Bahr, and G. Heppke, Mean-Field to Tricritical Crossover Behavior Near the Smectic-*A*–Smectic-*C** Tricritical Point, Phys. Rev. Lett. **61**, 547 (1988).

[55] J. A. Lipa, D. R. Swanson, J. A. Nissen, T. C. P. Chui, and U. E. Israelsson, Heat Capacity and Thermal Relaxation of Bulk Helium Very Near the Lambda Point, Phys. Rev. Lett. **76**, 944 (1996).

[56] D. J. Bishop and J. D. Reppy, Study of the Superfluid Transition in Two-Dimensional ^{4}He Films, Phys. Rev. Lett. **40**, 1727 (1978).

[57] Y.-J. Yun, I.-C. Baek, and M.-Y. Choi, Phase Transition and Critical Dynamics in Site-Diluted Josephson-Junction Arrays, Phys. Rev. Lett. **97**, 215701 (2006).

[58] S. Maat, J.-U. Thiele, and E. E. Fullerton, Temperature and field hysteresis of the antiferromagnetic-to-ferromagnetic phase transition in epitaxial FeRh films, Phys. Rev. B **72**, 214432 (2005).

[59] L. D. C. Jaubert and M. Udagawa, *Spin Ice*, 1st ed., Springer Series in Solid-State Sciences, Vol. 197 (Springer, Berlin, 2021).

[60] P. C. Guruciaga, S. A. Grigera, and R. A. Borzi, Monopole ordered phases in dipolar and nearest-neighbors Ising pyrochlore: From spin ice to the all-in–all-out antiferromagnet, Phys. Rev. B **90**, 184423 (2014).

[61] V. Raban, C. T. Suen, L. Berthier, and P. C. W. Holdsworth, Multiple symmetry sustaining phase transitions in spin ice, Phys. Rev. B **99**, 224425 (2019).

[62] W. Kwak, J. Jeong, J. Lee, and D.-H. Kim, First-order phase transition and tricritical scaling behavior of the Blume-Capel model: A Wang-Landau sampling approach, Phys. Rev. E **92**, 022134 (2015).

[63] K. Frye, S. Abend, W. Bartosch, A. Bawamia, D. Becker, H. Blume, C. Braxmaier, S.-W. Chiow, M. A. Efremov, W. Ertmer *et al.*, The Bose-Einstein condensate and cold atom laboratory, EPJ Quantum Technol. **8**, 1 (2021).

[64] S. K. Baek, P. Minnhagen, and B. J. Kim, Kosterlitz-Thouless transition of magnetic dipoles on the two-dimensional plane, Phys. Rev. B **83**, 184409 (2011).

[65] E. Y. Vedmedenko, N. Mikuszeit, H. P. Oepen, and R. Wiesendanger, Multipolar Ordering and Magnetization Reversal in Two-Dimensional Nanomagnet Arrays, Phys. Rev. Lett. **95**, 207202 (2005).

[66] D. Bitko, T. F. Rosenbaum, and G. Aeppli, Quantum Critical Behavior for a Model Magnet, Phys. Rev. Lett. **77**, 940 (1996).

[67] J. V. José, L. P. Kadanoff, S. Kirkpatrick, and D. R. Nelson, Renormalization, vortices, and symmetry-breaking perturbations in the two-dimensional planar model, Phys. Rev. B **16**, 1217 (1977).

[68] B. I. Halperin and D. R. Nelson, Theory of Two-Dimensional Melting, Phys. Rev. Lett. **41**, 121 (1978).

[69] D. R. Nelson and B. I. Halperin, Dislocation-mediated melting in two dimensions, Phys. Rev. B **19**, 2457 (1979).

[70] S. C. Kapfer and W. Krauth, Two-Dimensional Melting: From Liquid-Hexatic Coexistence to Continuous Transitions, Phys. Rev. Lett. **114**, 035702 (2015).

[71] M. Blume, V. J. Emery, and R. B. Griffiths, Ising model for the λ transition and phase separation in He^3−He^4 mixtures, Phys. Rev. A **4**, 1071 (1971).

[72] J. B. Santos-Filho and J. A. Plascak, Monte Carlo simulations of the *XY* vectorial Blume-Emery-Griffiths model in multilayer films for ^{3}He - ^{4}He mixtures, Phys. Rev. E **96**, 032141 (2017).

[73] C. Kaspar, B. Ravoo, W. van der Wiel, S. Wegner, and W. Pernice, The rise of intelligent matter, Nature (London) **594**, 345 (2021).

[74] A. Walther, From responsive to adaptive and interactive materials and materials systems: A roadmap, Adv. Mater. **32**, 1905111 (2020).

[75] A. Blomqvist, G. K. Pálsson, C. M. Araújo, R. Ahuja, and B. Hjörvarsson, Significance of Self-Trapping on Hydrogen Diffusion, Phys. Rev. Lett. **105**, 185901 (2010).

[76] S. Bhanja, D. Karunaratne, R. Panchumarthy, S. Rajaram, and S. Sarkar, Non-Boolean computing with nanomagnets for computer vision applications, Nat. Nanotechnol. **11**, 177 (2016).